nature materials

Supplementary information

https://doi.org/10.1038/s41563-025-02154-5

Ultrafast evanescent heat transfer across solid interfaces via hyperbolic phonon–polariton modes in hexagonal boron nitride

In the format provided by the authors and unedited

Table of Contents

A. Visible Pump, Infrared Probe Measurements

In order to study the ultrafast heat transfer processes of the optical phonons in hBN after thermal coupling with the Au pad via evanescent heat transfer, we utilize a home-built ultrafast pump-probe system with tunable probe wavelengths. Our experiment is built around a regenerative amplified laser system (Spectra Physics SPIRIT) emanating ~400 fs, 1040 nm pulses at a repetition rate of 500 kHz. The output of this laser is directed into two paths, the “pump” and “probe”. The pump path is frequency doubled to 520 nm then passed down a mechanical translation stage, which changes the path length with respect to the probe pulse; in our configuration, we shorten the delay line of the pump with respect to the probe to generate our transient reflectivity data. The pump pulse train is then chopped at a rate of 451 Hz and focused onto the sample surface at the patterned flake of interest. The probe pulse gets fed through a mid-Infrared (MIR) optical parametric amplifier (OPA) which then outputs a range of frequencies from 2-16 microns. The OPA splits the seed laser into two paths the first is used as an high energy pump (520nm, the second harmonic of the seed) which is primarily used for power amplification of the seed, after this amplification step the seed is referred to as the signal beam (680-840nm) and is used in mixing to generate the desired output, the second path is sent though a white light generation (600 -1100nm, WLG) crystal and is subsequently used for the process of seed amplification. The amplification step results in additional photons which constitute the Idler beam (1350-2060nm), these three beams have a simple relationship (below) between their wavelengths given by the conservation of energy.

$$\frac{1}{\lambda_{idler}} = \frac{1}{\lambda_{pump}} - \frac{1}{\lambda_{signal}} \quad (1)$$

A similar process of amplification is repeated using the Idler (1350-2060nm) from the first amplification step, the Idler from the second amplification step and the fundamental seed (1040nm residual after the SHG), resulting in tunable Signal (1350-2060nm) and Idler (2060-4500nm) beams. This tunability is derived from the spectral overlap of the pump and WLG pulses in the first amplification step. The two beams resultant from the final amplification step can finally be combined into a difference frequency generation (DFG) crystal for tunable output from 4-16 μm. For our work, we filter the Idler and Signal out of the path using a Germanium window and use wavelength from the DFG as the probe, allowing us to access probe wavelengths at 15 nm increments through a range of 5-9 mm to measure across the Reststrahlen band in hBN[1-3]. This probe is then focused onto the sample surface, centered around the pump (Fig. S1).

The patterned hBN flake is oriented on a sample holder such that the probe light incident on the surface is p-polarized. P-polarized light was chosen somewhat arbitrarily to due to physical limitations on the measurement table. Transfer matrix method calculations (detailed in section B) were used to assure that the signals would be polarization independent confirmed in Figs. S2 and S3. The reflection of the TO observed is most similar across polarizations at 45 degrees (Fig. S3) so to get consistent signal an angle of 45 degrees was used in our measurements. The reflected probe signal is then measured by a MCT photo detector sensitive to our frequency range (Vigo PC-4TE-14-1x1). We lock in to the probe pulse signal at the chopper frequency of the pump as a function of pump-probe delay time. We monitor this transient thermoreflectivity at different probe wavelengths, generating the wavelength dependent transient pump-probe contour plots, shown in Figs. S4 and S5. Each experiment was repeated 5 times over 2 flakes

with different patterning. The additional spectral sweep on an 89nm sample flake is shown in Fig. S6. Showing a similar ultrafast heating of the Reststrahlen band.

To better understand our measured signal several backgrounds were taken to filter out the substrate and transducer effects. These scans, summarized in Figs. S4 and S5, show that there is only a very minor spectrally independent response from Au at the wavelengths of interest which is consistent with the low thermoreflectance at IR wavelengths reported in literature[4]. There does seem to be some response from the Silicon substrate, but the region that this appears is near the edge of the hBN Reststrahlen band so our mechanism should be shielded from the noise caused by this. This is further supported from the data shown when the probe wavelength lies outside of the Reststrahlen band, which is indicative of the response of the silicon substrate from the thermal discharge of the Au; as expected, at the early timescales, the heating of the Si from the Au should be negligible.

B. Optical Modelling

To determine the spectral response of the hBN, Transfer Matrix method (TMM)[5] calculations were performed on simulated stacks of hBN(116nm)/SiO_2(280nm)/ Si(0.5mm) with and without a prism layer assuming incident photons on the hBN. The Au pattern was neglected from the model as the addition does not add accuracy since the spectral variation of the dielectric function of Au at these wavelengths is negligible[6]. Due to the nature of our experiment, some minor changes were made to the method for a direct comparison to our measured signal.

The first change was made to mimic the thermoreflectivity response that we measure, which is a differential signal that measures the change in probe reflectivity due to a thermal perturbation. For this, we perform two separate calculations, the first being made to an unpumped stack where all optical constants are drawn from literature (see Table S1),[1] and the second calculation made to a perturbed case, where the optical parameters in the dielectric function of hBN were adjusted slightly from their "unpumped" values. For the dielectric function of hBN, a Lorentz oscillator model was used with a "TOLO" form as below[1],

$$\varepsilon(\omega) = \varepsilon_\infty \left(\frac{\omega_{LO}^2 - \omega^2 - i\Gamma\omega}{\omega_{TO}^2 - \omega^2 - i\Gamma\omega} \right) \quad (2)$$

where ω is the frequency and the subscripts LO and TO denote the longitudinal and transverse phonon frequencies, respectively, *G* is the damping, and ε_∞ is the high frequency permittivity. The difference between our unpumped and pumped TMM calculations yield "DR", which is then divided by the unperturbed calculation to mimic the

reported “DR/R” of our measurements. In order to fit these TMM predictions to our measured data, a nonlinear least squares fit was performed by tuning the optical constants of the perturbed calculation.

The second change made to a traditional TMM approach was to accommodate the anisotropic nature of hBN. The dielectric function was separated even further into $\varepsilon_{\perp}$, and $\varepsilon_{\parallel}$ with similar TOLO forms as above. These two different dielectric functions allow for a unique treatment for each of the ordinary and extraordinary axes. The calculations used followed closely the 4x4 Transfer matrix formalism outlined by Ref.[5].

We noted that the TMM calculations described above could not effectively represent the data at early times with any reasonable changes (S7). This led to the addition of a prism layer to our stack to better encapsulate the polariton being active in the system. The prism slightly bends the light line to better momentum match to the polariton dispersion in the hBN. In the simulation this effect is incorporated with a layer of material above the hBN flake with a flat refractive index of 1.7 across the spectra. This value was settled on as it bent the incoming light enough to mesh well with our measured spectra without distorting the spectral shape too much. The result of fitting both simulations to the data at several different temporal cross sections is shown by Fig. S7. The most significant changes required to fit the signal were in the epsilon infinity of hBN as well as the TO phonon frequencies, which both are direct indications of thermal changes in the hBN. These frequencies were confirmed to be HPhP modes via accompanying s-SNOM measurements (S8).

The temporal dynamics of the model parameters trend similarly to the signal; the changes in the parameters increase to a maximum at a delay time of approximately 45ps

and then decay until 1800ps. This trend is expected as the model parameters reflect the temperature of the system. To this point, the parameters change smoothly across the time delay, that is, there are no sharp changes to the fitted parameters above the large gradient near 45ps, which is associated with the ultrafast heating of the hBN surface. The least squares fitting procedure randomly perturbs the values of the model in search of the smallest residual between the data and the model. However, the final fit for every simulated time delay follows the expected temperature trends from heating. From our fits, we observe a shift in TO frequency and an increase in the dampening parameter as the temperature rises. This aligns with our physical expectations, as when the temperature increases, the frequency of the TO mode shifts due to the thermal expansion of the bonds, changing the energy of the mode. Additionally, at higher temperatures, the total number of active modes in the system increases, which intensifies the scattering of the optical modes, resulting in the broadening of the peaks and an increase in the dampening parameters.

C. Temporal Modelling

The first model we used to fit our data was a solution to the cylindrical heat equation using code typically used for standard TDTR data[7]. Figure S9 was created by exploring the entire space of enhanced TBCs as well as effective in-plane polariton conductance that could possibly represent the data. The curves are isolines of constant mean squared error. This illustrates that the best fits lie within the solid 0.05 isoline and highlights this models' insensitivity to the thermal boundary conductance as the value increases beyond 500 as all of these values fit within 5% error. Thus, this model serves as a proof for the enhancement of TBC and thermal energy transfer between Au and hBN. We have provided additional calculations in Fig. S12 and S11 for the surface temperatures of the Au and hBN in our analytical models. Without the high boundary conductance, the thermal model cannot predict the extreme curvature at early times (500-1000ps). The in-plane polariton conductance is altered to match the slope trends at longer times (<1000ps). Our analysis estimates the temperature of the surface of hBN based on the solution to the cylindrical heat equation applied to a multilayer geometry, a typical approach used for analyzing pump-probe thermoreflectance experiments in the time. We modified the model to account for our experimental conditions. Laser repetition rate was adjusted from 80MHz to 500-kHz matching our seed laser repetition rate. Our system was also modulated at much lower frequencies from TDTR (300Hz). To simulate the small pumping region in our model (the gold radiator pad), we restricted the heat flow to solely cross-plane transport regulating the flux by perturbing the TBC alone. To capture the anisotropic heat transfer of the hyperbolic modes, we perturbed the in-plane thermal conductance of the hBN layer. When fitting our data, we held the cross-plane thermal conductivity

constant and varied the in-plane conduction as well as the Au/hBN interfacial conductance. A least squares fitting algorithm was then performed perturbing the fit variables. In our simulations, the temperature curve associated with the hBN was spatially averaged over the size of the entire flake.

The authors recognize that this purely diffusive model is insufficient in quantifying energy transfer rates that occur on photonic timescales.

To remedy this shortcoming, we devise a two-temperature model that can isolate the TBC and get us to a better approximation. In our pump-probe measurement, electrons are excited within gold with a sub-picosecond pulse and upon excitation, heat is transferred ballistically to the gold-boron nitride interface. Because electron-phonon nonequilibrium in gold has a duration on the order of tens of picoseconds and the lifetime of optical phonon modes are on the order of hundreds of picoseconds, we consider our model as a lumped capacitance model with a single temperature in both gold and boron nitride. [8]Thus, for this model we use a parabolic one step model (POS) to model the thermoreflectance data for probe energies within the Reststrahlen band of hBN that is shown by the following differential equations:

$$C_{AU}(T_{AU})\frac{\partial T_{AU}}{\partial t} = -\frac{h}{d_{au}}(T_{AU} - T_{HBN}) \quad (3)$$

$$C_{HBN}(T_{HBN})\frac{\partial T_{HBN}}{\partial t} = \frac{h}{d_{au}}(T_{AU} - T_{HBN}) + \nabla \cdot (\kappa_{HBN}\nabla T_{HBN}) \quad (4)$$

$$C_{HBN}(T_{HBN})\frac{\partial T_{HBN}}{\partial t} = \nabla \cdot (\kappa_{HBN}\nabla T_{HBN}) \quad (5)$$

where h represents the thermal boundary conductance (TBC) between phonons in gold and optical phonons in boron nitride, d_{au} represents the thickness of gold, κ_{HBN} represents

the thermal conductivity of boron nitride, and T_{AU} and T_{HBN} represent the temperatures of gold and boron nitride respectively.[9,10] Equation 3 describes the thermal transport in Au where we assume that the gold depth has thermalized within the pulse duration, as the ballistic penetration depth of gold is larger than the 50 nm Au used in our experiment. [11] Thus, the only term describing thermal transport in Au is the thermal boundary conductance from gold to optical phonons in boron nitride. Equation 3 describes the Au/hBN interface node. Equation 4 describes the thermal transport within hBN where we discretize the thickness of each hBN flake into 0.5 nm step sizes.

In order to remove source term uncertainties, we normalize the temperatures in Eqs. (3), (4), and (5), to take the following form[12]:

$$\varphi_{f,s} = \frac{T_{f,s} - T_0}{T_f(0) - T_0} \tag{6}$$

where T_0 is the temperature of the film and the substrate before excitation, $T_f(0)$ is the temperature of the film immediately after excitation, and $T_{f,s}$ is the unnormalized temperature distribution. This results in the POS model taking the following form:

$$C_{AU}(\varphi_{AU})\frac{\partial \varphi_{AU}}{\partial t} = -\frac{h}{d_{au}}(\varphi_{AU} - \varphi_{HBN}) \tag{7}$$

$$C_{HBN}(\varphi_{HBN})\frac{\partial \varphi_{HBN}}{\partial t} = \frac{h}{d_{au}}(\varphi_{AU} - \varphi_{HBN}) + \nabla \cdot (\kappa_{HBN}\nabla\varphi_{HBN}) \tag{8}$$

$$C_{HBN}(\varphi_{HBN})\frac{\partial \varphi_{HBN}}{\partial t} = \nabla \cdot (\kappa_{HBN}\nabla\varphi_{HBN}) \tag{9}$$

Subject to the following conditions in replacement of a source term:

$$\varphi_{AU}(0, t_0) = 1 \tag{11}$$

$$\varphi_{HBN}(\infty) = 0 \tag{12}$$

where t_0 represents the time, the sample starts heating. In our model we set t_0 to the time of the max thermoreflectance signal for each dataset. The constants for our two-layer model can be found in Table S3 and sensitivities for each fitting parameter can be found in Fig. S10.

The temporal dependence in interface-mediated radiative polaritonic heating is further solidified by analyzing the temporal changes in the experimental data within this parabolic one step model (POS) framework. For this model we needed to introduce new values to our calculations that correspond to the heat capacities of the optical phonon branches as well as thermal conductivities for each; all values used in this calculation are detailed in Table S4. A Debye model was used to approximate the boron nitride optical phonon heat capacity. This made it possible for us to only use one unknown parameter for fitting (Fig. S10), an effective thermal boundary conductance (TBC) from the bulk heat carriers of gold to the optical phonon-polariton modes of hBN. We also allowed for a 20 percent perturbation in thermal conductivity when fitting in order to better capture our data.

We begin our fits at a time of t = 100 ps as to not be sensitive to uncertainties associated with initial laser source heating and to be sufficiently after the equilibration time of electrons and phonons in gold.[13,14] Using an estimated PBC value of 1 GW/m^{2}K in addition to our calculated optical phonon heat capacity and measured hBN flake thicknesses.[12]

Additionally, the POS predicts a temperature rise on the order of 8K. This temperature is indicative of the maximum temperature rise of the lattice in our experiment, however at these lattice temperatures the optical modes are all frozen out (shown in main text). In order to obtain a sufficient activity of the TO phonon we needed to artificially heat the

system upwards of 1000 K which implies that there is some non-thermal excitation of the optical modes, which in our case is attributed to polaritonic coupling.

D. TDTR Measurement of Au/hBN Boundary Conductance

To prepare samples for TDTR we first deposit an 50nm thick Au transducing layer via electron beam evaporation at 7 μTorr on each of 2 samples with at least one exfoliated (see methods) flake for measurement. This sample stack was chosen to isolate the Au/hBN TBC and remaining as close to the active experiment as possible. This technique utilizes sub-picosecond pulses emanating from a Ti-Sapphire oscillator at 80MHz repetition rate. The pulses are separated in a pump path and a time delayed probe path that is reflected from the Au transducer. Both paths are tinted before the sample such that the pump can be filtered out before collection. The probe beam effectively measures the change in thermoreflectivity of the surface of the transducer tracking the decay of thermal energy deposited by the pump pulse. The pump line is modulated by an Conoptics electro-optic modulator in order to demodulate the ratio of in-phase and out-of-phase reflected probe signal ($-V_{in}/V_{out}$) via lock in detection at the pump modulation frequency. The signal is recorded for atleast 5ns after the pump heating event, this characterizes the thermal decay sufficiently for thermal analysis. Three modulation frequencies (1MHz, 5MHz, 8MHz) were chosen to maximize sensitivity to the Au/hBN TBC (G1) (see Fig. S12). S18 was calculated by solving the cylindrical heat equation varying modulation frequency and simulating the distributions of thermal gradients in the sample stack. Then by varying each of the desired fitting parameters by 0.1% and subtracting the original decay curve then normalizing by the magnitude of the perturbation allows for a direct comparison of the relative “strength” of each parameter.

Visualizing this “strength”, commonly called sensitivity, allows the experimenter to select the measurement scheme to isolate desired parameters. For example, in S18 it is shown that the buried interface resistance (G_2) is relatively insensitive in our sample stack thus, no matter the quality of the hBN/SiO2 interface, other parameters like G_1 and the cross plane thermal conductivity of hBN (k_2) can still be fit. Using two different samples of different hBN thicknesses (89nm, and 195nm) allowed us to normalize the effect of the competing resistances out and hold TBC constant across samples.

On all TDTR samples the most sensitive parameters are the thermal conductivity and thickness of the transducer, so these two values are measured rigorously after deposition via characterization of a witness sample present in the deposition. The thickness is measured via profilometry, and the thermal conductivity is measured via four-point resistivity[15] and conversion to thermal conductivity using the Wiedemann Franz law[16]. The pump and probe beams are focused on the Au Transducer at e^{-2} radii values of 12 and 9 μm for the pump and probe spots respectively. Each sample was measured 3 times at each modulation frequency to reduce systematic error. Then using a numerical solution to the cylindrical Heat Equation[17] a contour is fit to all nine datasets at once is found (89nm sample shown in Fig. S13) with fitted and assumed Thermal parameters with significant sensitivity are listed in table S4. In an effort to quantify the error of each measurement the fitting procedure is repeated after varying all sensitive thermal parameters by up to 10% and calculating the square root of the sum of all the squares of resultant errors (see Table S4).

E. Ultrafast Pump-Probe Response of Au on Silicon and hBN Substrates

To demonstrate the role of polaritonic interfacial heat transfer on the transient temperature changes of Au, we pump the Au with a 520 nm pump pulse and probe the resulting transient thermoreflectance using a 2.1 mm probe pulse. The first ~10 ps during/after 520 nm pump heating represent the time scale where the electron and phonons in the Au are out of equilibrium with each other and, assuming no energy loss to the substrate, the cooling of the electrons in the Au/heating of the lattice in the Au is driven nearly entirely from electron-phonon coupling in the Au (G). This is a well-established process that is captured with the two-temperature model on these time scales. In our experiments, we use 50 nm Au/silicon as this control, with this ultrafast data shown in Fig. S15 (a) below. We note at these probe wavelengths, the thermoreflectivity is related to the Drude response[23,24], as previously mentioned, and subsequently, our thermoreflectivity data in Au is directly related to the lattice temperature profile, so hence, in these data, we are measuring the Au lattice heat up during/after nonequilibrium heating and subsequent electron-phonon coupling in the Au. The using the TTM fit to this data (best fit shown in Fig. S15), we extract an electron-phonon coupling factor of Au as $G = 4.0 \times 10^{16}$ W m^{-3} K^{-1}, which is in good agreement with prior values measured for high fluence short-pulsed laser heated Au on silicon (i.e., when the degree of electron-phonon nonequilibrium in the Au is large; stated differently, when the effective electronic temperature is on the order of 1000's of K prior to equilibration with the lattice).[25] We note in this TTM fit, we only adjust G and no other parameter in the model. Fig. S15(b)

illustrates the raw magnitude of the data taken from the scan shown in Fig. S15(a). The Au seems to be dramatically cooler in the case of the hBN substrate, strengthening the evidence for the ultrafast cooling mechanism described in the main text of the manuscript. Fig. S15(c) adds additional context to the cooling of the Au surface in Fig. S15 at longer time delays. We can see that at significantly long time delays after the mechanism the dominant thermal baths return to the diffusive phonon processes as expected from the thermal gradients in a transducer past 100ps

As shown in Fig. S15 (a), when comparing the transient lattice temperature changes in Au when on a Si substrate to those when on a hBN substrate, the Au lattice temperature changes during and after 520 nm pump heating are suppressed at shorter pump-probe delay times and take longer to rise and equilibrate when coupling to the excited electrons in the Au. This can be qualitatively understood as a parallel energy pathway to electron-phonon scattering in the Au. This parallel thermal transport pathway is the hot electrons in the Au evanescently coupling to HPhP's in the hBN via the NFRHT mechanism that we have observed in the main manuscript. We note that this pathway is available in the polar hBN substrate that supports phonon polaritons but not the non-polar Si substrate. To quantify this, we then fit these data with a three-temperature model, which in addition to electron and phonon energy transfer in the ultrafast laser heated Au, we now include an additional coupling pathway from the electrons in the Au to the optical phonons in the hBN.[25-27] The calculations for this three-temperature model assuming gold electron to hBN thermal boundary conductance of 500 MW m^{-2} K^{-1} (similar value to that fit when probing the hBN directly in the main manuscript) is shown in Fig. S15(a), showing agreement with the trends in the Au/hBN experimental data. Again, this suppressed and

delayed ultrafast lattice temperature rise in the Au/hBN data as compared to the Au/Si data can only be captured by assuming Au electrons can lose energy to the hBN. Note, in this 3TM model, we use all the same parameters used in the Au/Si TTM fit to describe the electron and phonon energy transport within the Au in the 3TM model. These data demonstrate that the ultrafast thermal dynamics of Au are impacted on hBN substrates due to this HPhP interfacial energy transport mechanism.

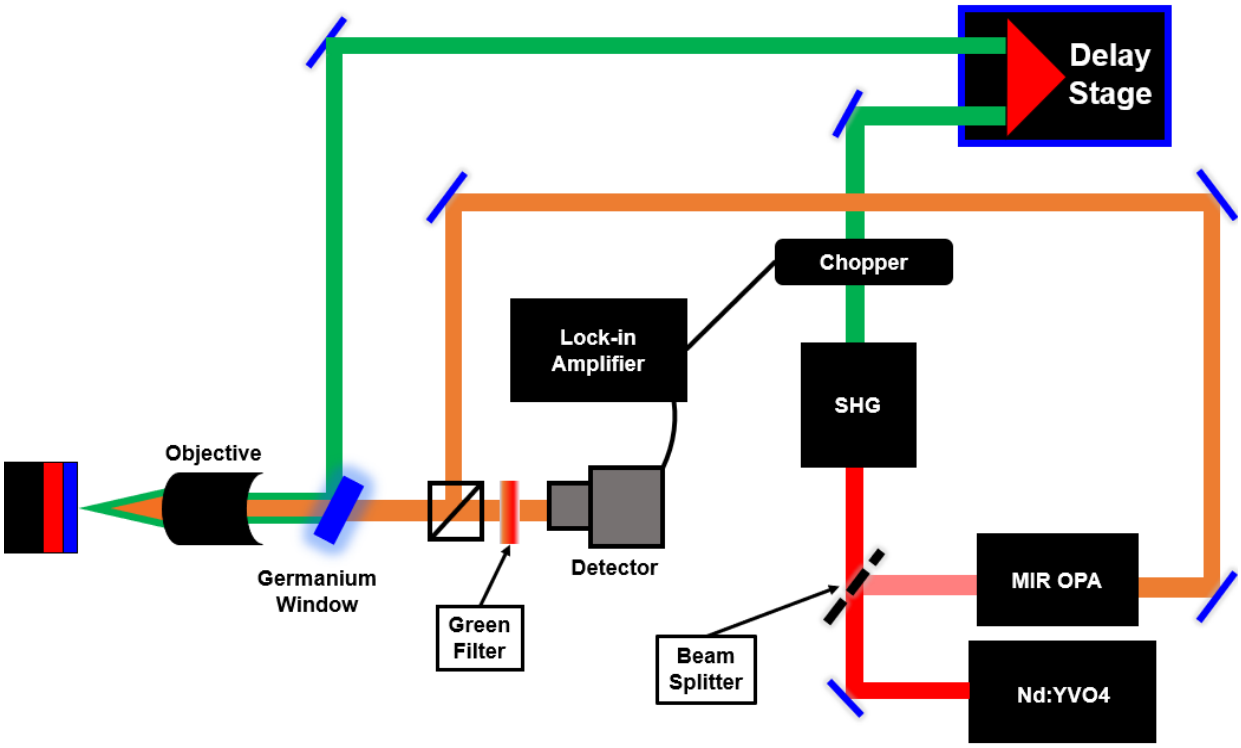

Figure S1: A diagram of the MIR pump probe technique.

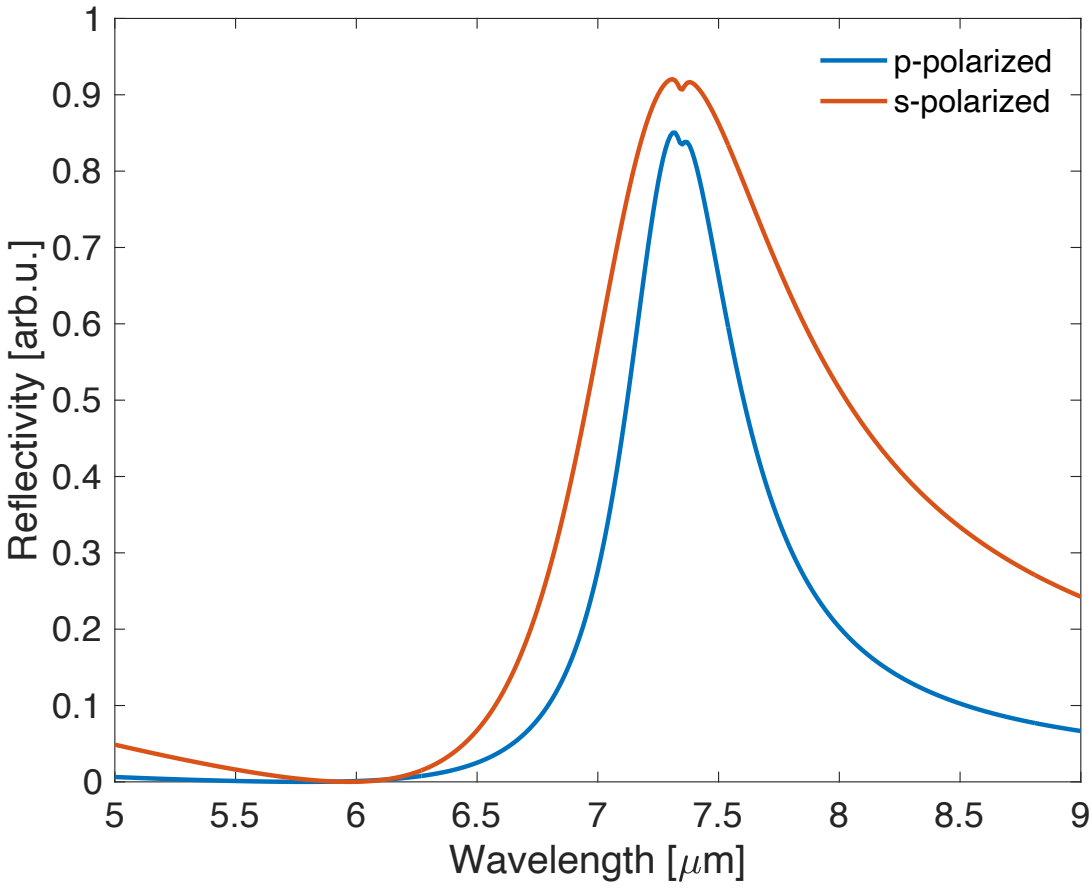

Figure S2: TMM simulation comparing the 45 degree reflectance of hBN within the Reststrahlen region displaying the similarity in signal.

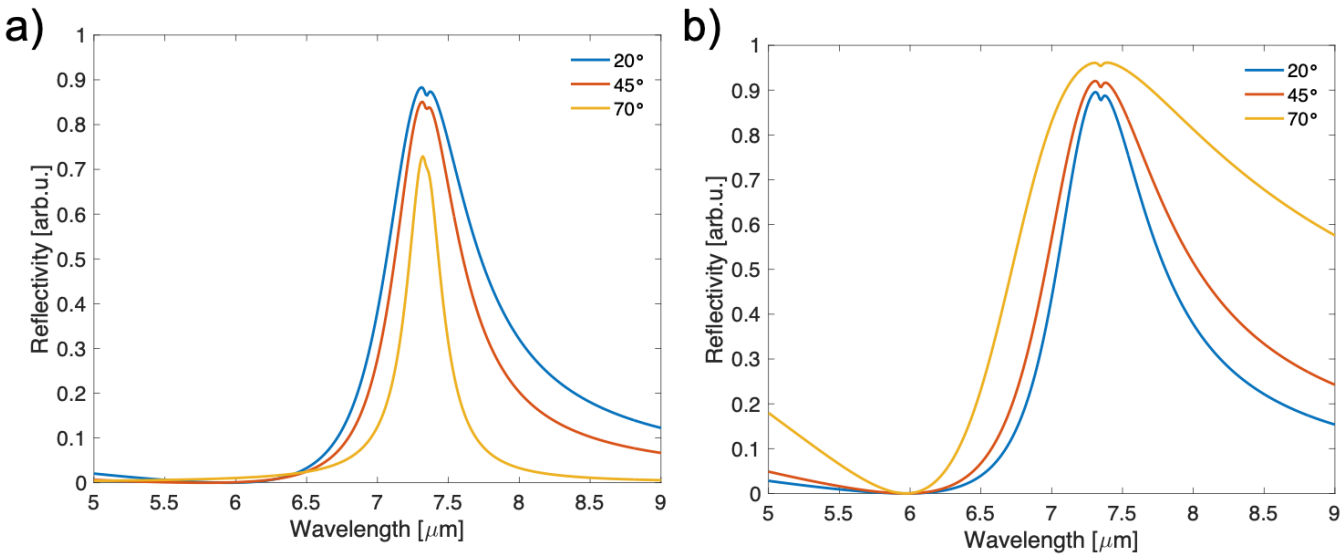

Figure S3: TMM simulations comparing the angle dependences for (a) p-polarization and (b) s-polarization showing commonality of signals at near 45 degree angles but high variability at angles >70 degrees.

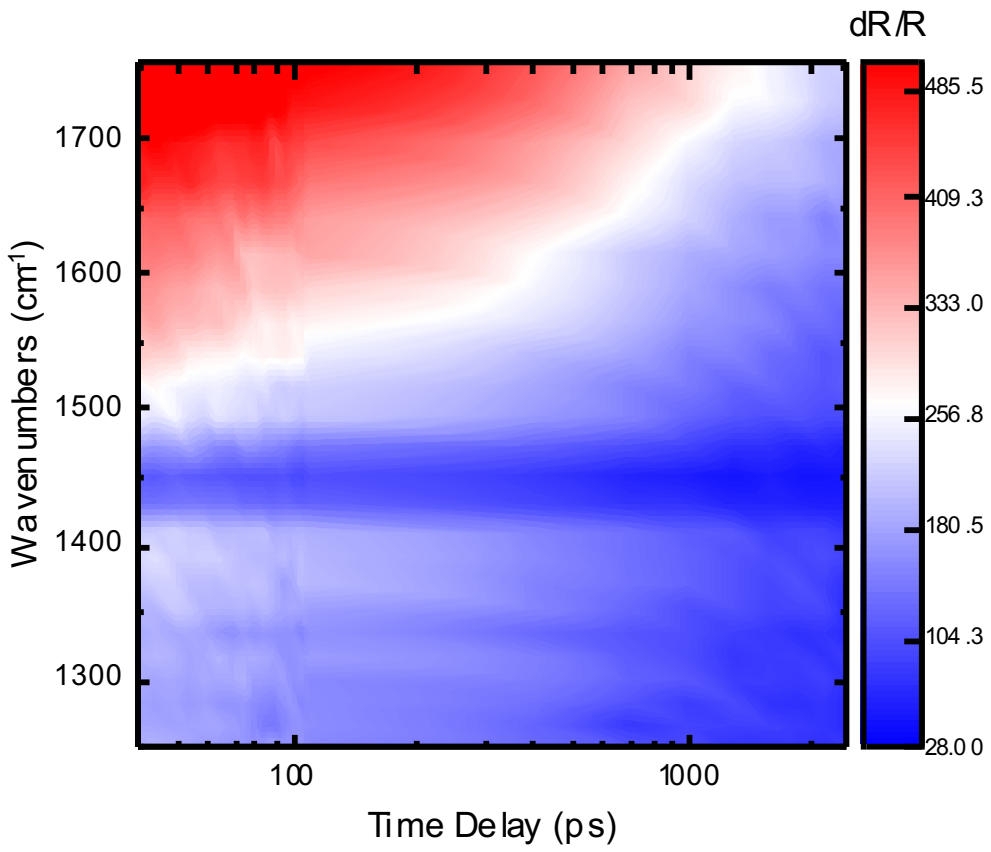

Figure S4: A contour of an uncoated hBN flake.

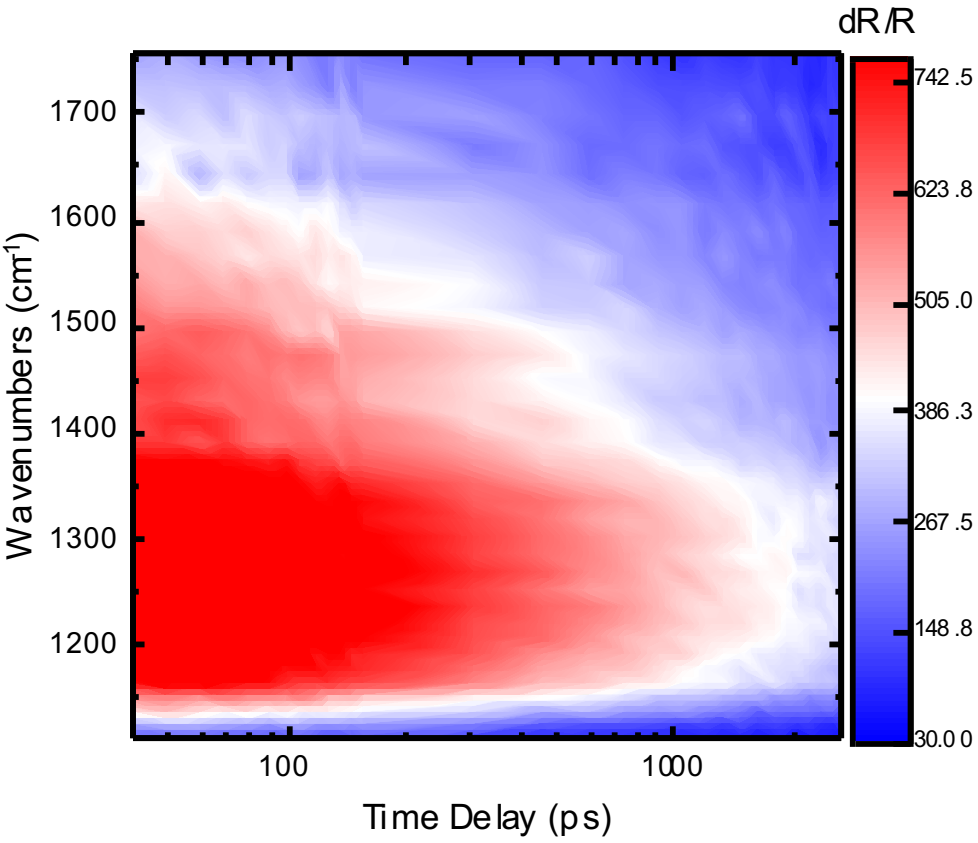

Figure S5: This shows a sweep on the substrate beside a patterned hBN flake to determine a direct background.

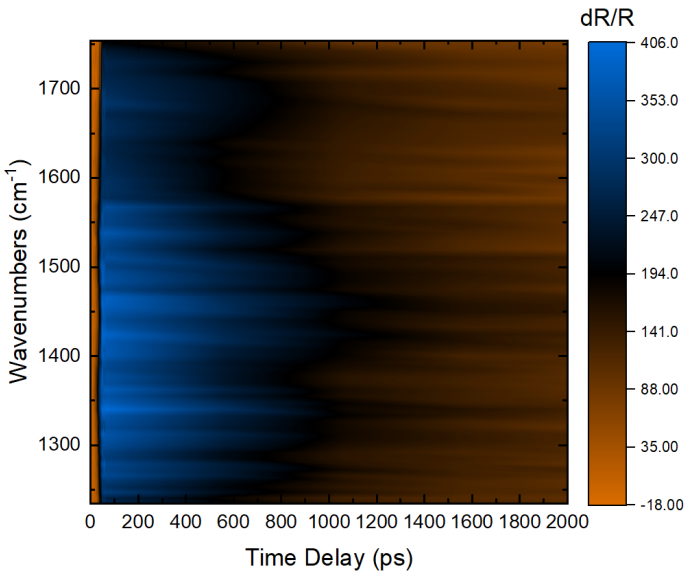

Figure S6: Measured ΔR/R spectra taken from a separate flake with a thickness of 89 nm.

Table S1: Summary of unperturbed values considered in the TMM calculations. These values were also used as the starting point for the fitting procedure.

^{11}B 99.2%	ε_∞	$\omega_{TO}(cm^{-1})$	$\omega_{LO}(cm^{-1})$
Ordinary axis[1]	5.32	1359.8	1608.7
Extraordinary Axis[1]	3.15	755	814

Table S2: an overview of the perturbations fitted parameters given as a percentage for each of the terms in the TO-LO form of the dielectric function for both the in plane and cross plane directions.

	Prism(%)	Prisimless(%)
$\Gamma_{\perp}$	10-15	5-12
$\Gamma_{\|\|}$	2-4	1-2
$\omega_{LO\perp}$	0-1	0-1
$\omega_{TO\perp}$	10-13	0-1
$\omega_{LO\|\|}$	20-30	5-13
$\omega_{TO\|\|}$	4-5	4-5

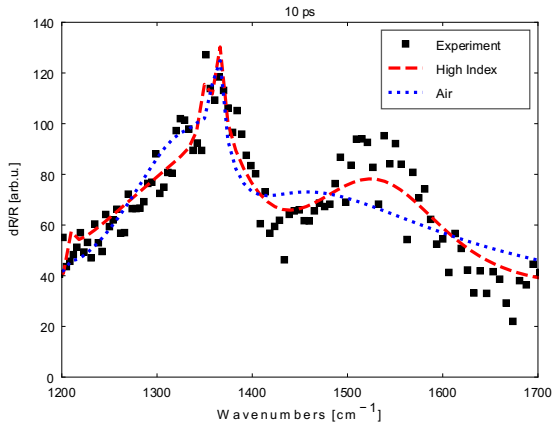
10 ps
Experiment
High Index
Air
dR/R [arb.u.]
Wavenumbers [cm^{-1}]

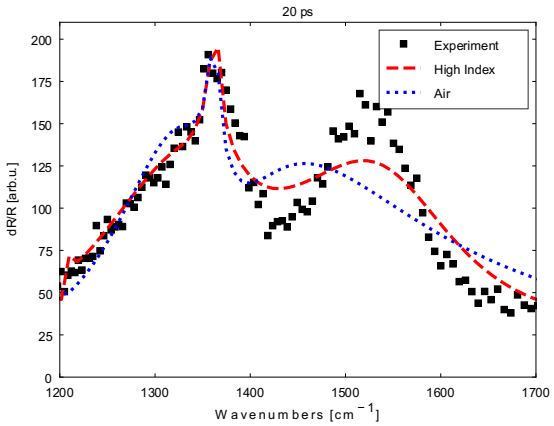
20 ps
Experiment
High Index
Air
dR/R [arb.u.]
Wavenumbers [cm^{-1}]

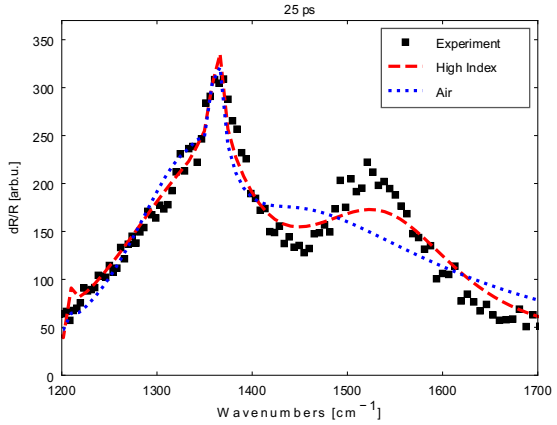
25 ps
Experiment
High Index
Air
dR/R [arb.u.]
Wavenumbers [cm^{-1}]

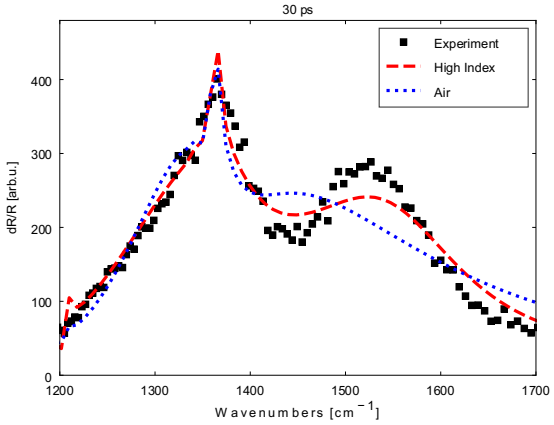
30 ps
Experiment
High Index
Air
dR/R [arb.u.]
Wavenumbers [cm^{-1}]

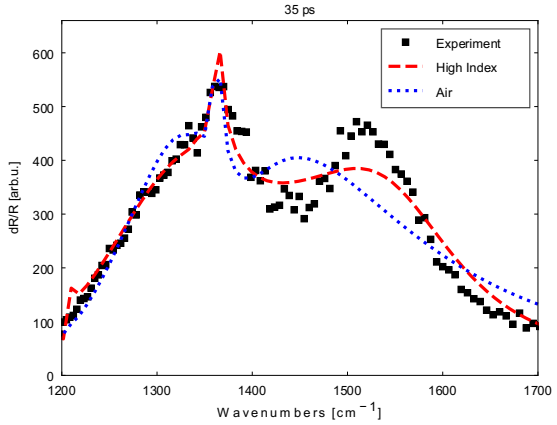
35 ps
Experiment
High Index
Air
dR/R [arb.u.]
Wavenumbers [cm^{-1}]

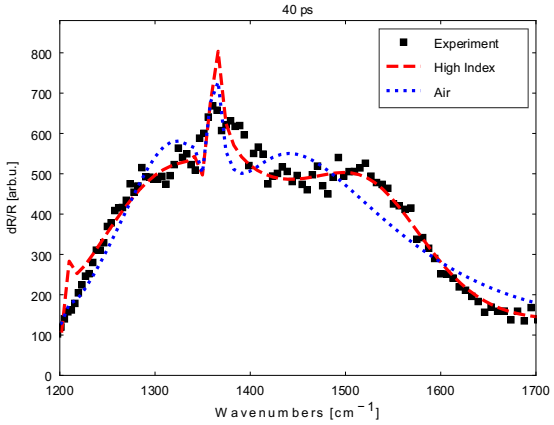
40 ps
Experiment
High Index
Air
dR/R [arb.u.]
Wavenumbers [cm^{-1}]

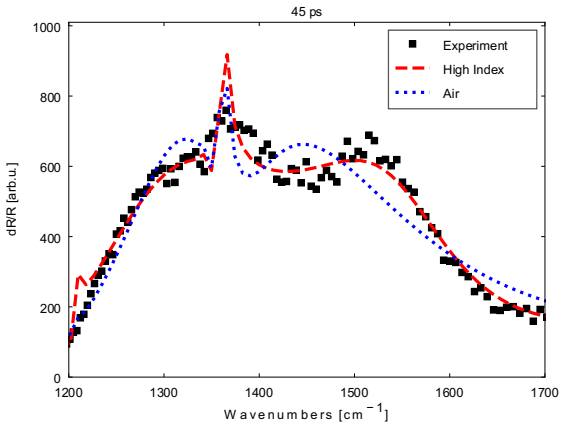
45 ps
Experiment
High Index
Air
dR/R [arb.u.]
Wavenumbers [cm^{-1}]

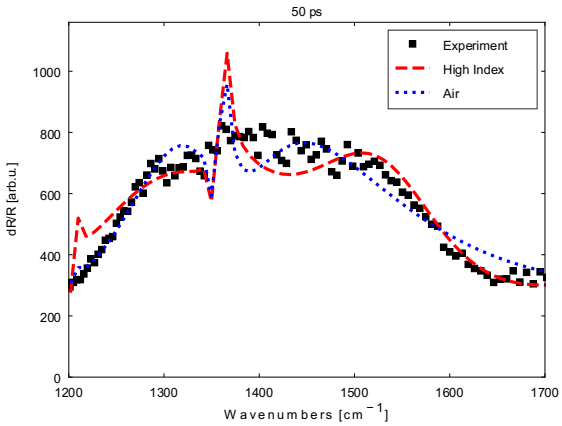
50 ps
Experiment
High Index
Air
dR/R [arb.u.]
Wavenumbers [cm^{-1}]

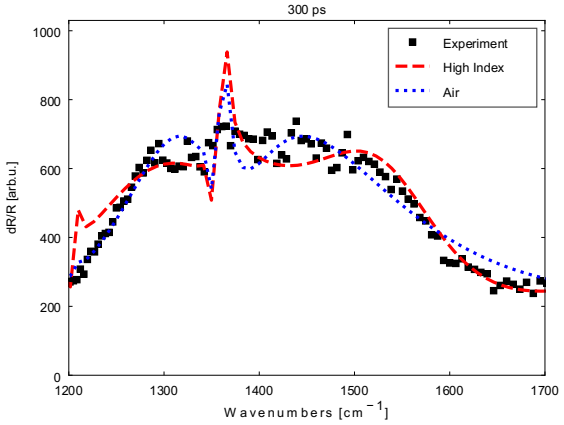
300 ps
Experiment
High Index
Air
dR/R [arb.u.]
Wavenumbers [cm^{-1}]

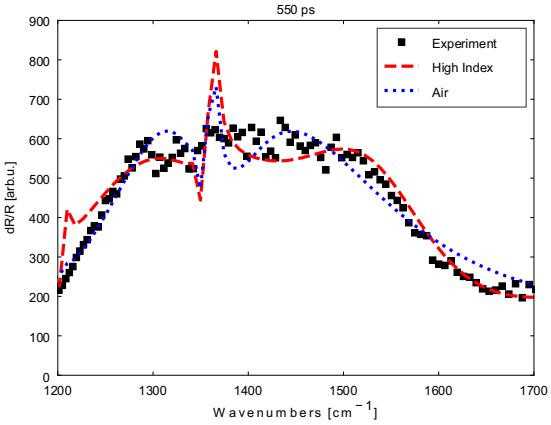
550 ps
Experiment
High Index
Air
dR/R [arb.u.]
Wavenumbers [cm^{-1}]

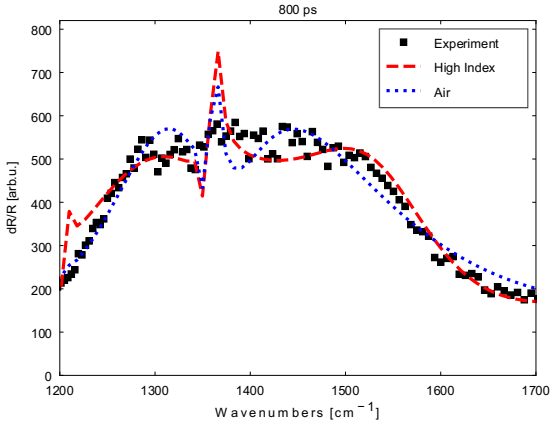
800 ps
Experiment
High Index
Air
dR/R [arb.u.]
Wavenumbers [cm^{-1}]

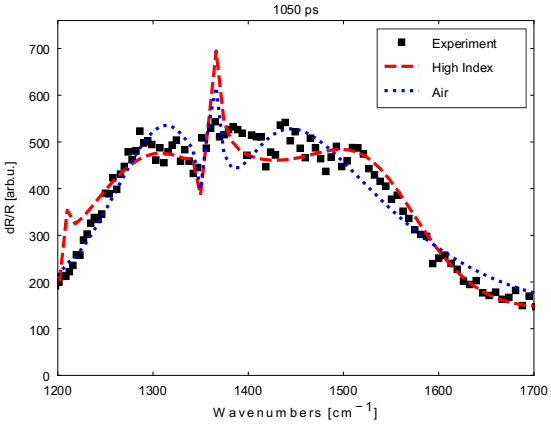
1050 ps
Experiment
High Index
Air
dR/R [arb.u.]
Wavenumbers [cm^{-1}]

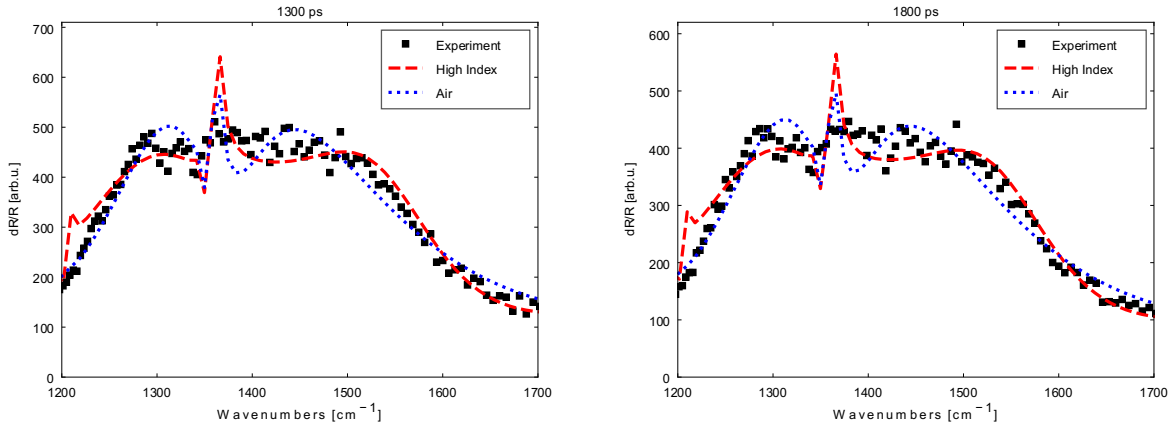

Figure S7: ***Comparison of the measured thermoreflectance data to high-index model and the prisimless air model at time delays of 10-1800 ps.*** *We see preferential heating of the modes associated with the high-wavevector HPhPs for early time delays (10-45 ps) which is an order of magnitude faster than the rates of conduction should allow. This significant heating event also left a thermal signature for all time delays measured, highlighting the timescale of thermal phonon modes in the wake of ultrafast HPhPs.*

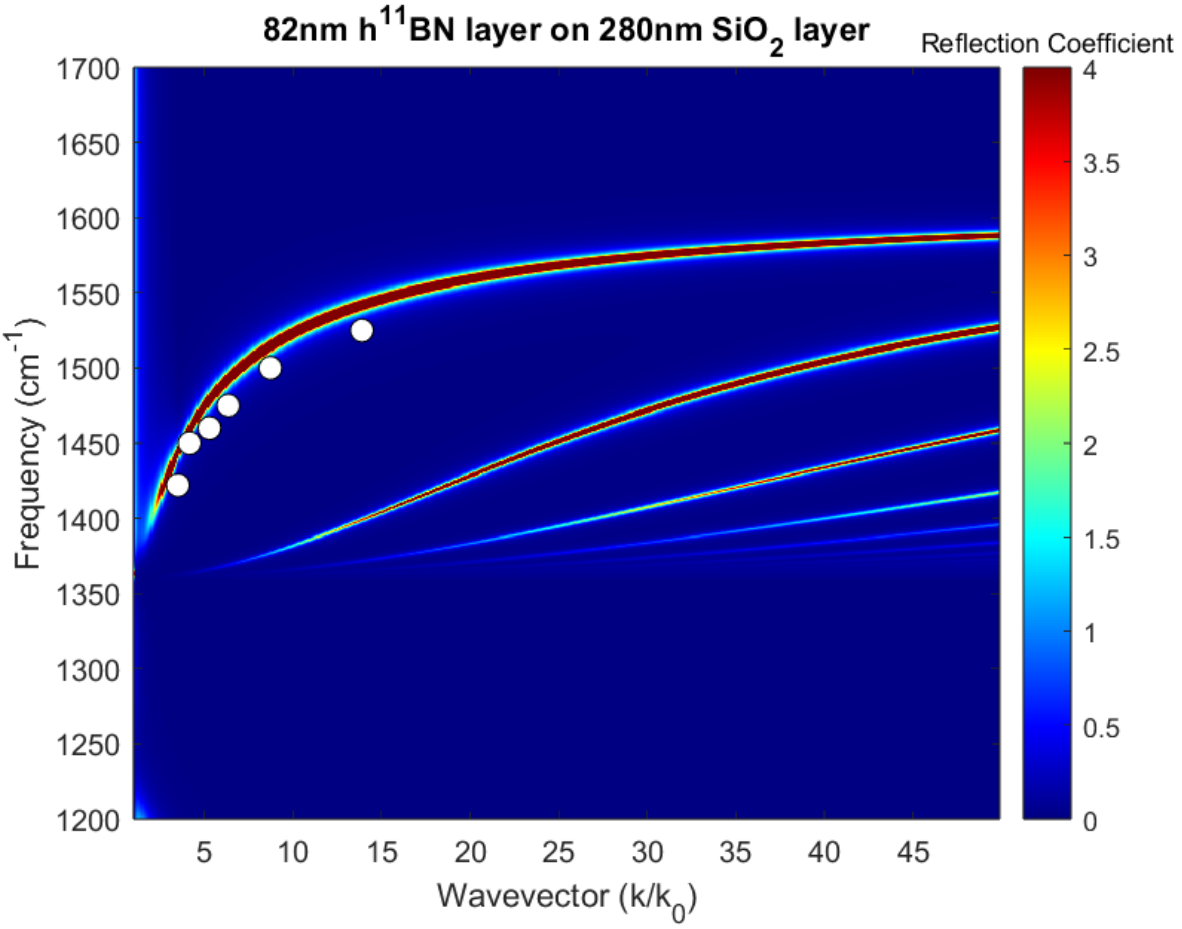

Figure S8: ***Measured s-SNOM signal.*** *The Solid white dots are measured s-SNOM data. The main contour is a calculated dispersion of the HPhPs of hBN.*

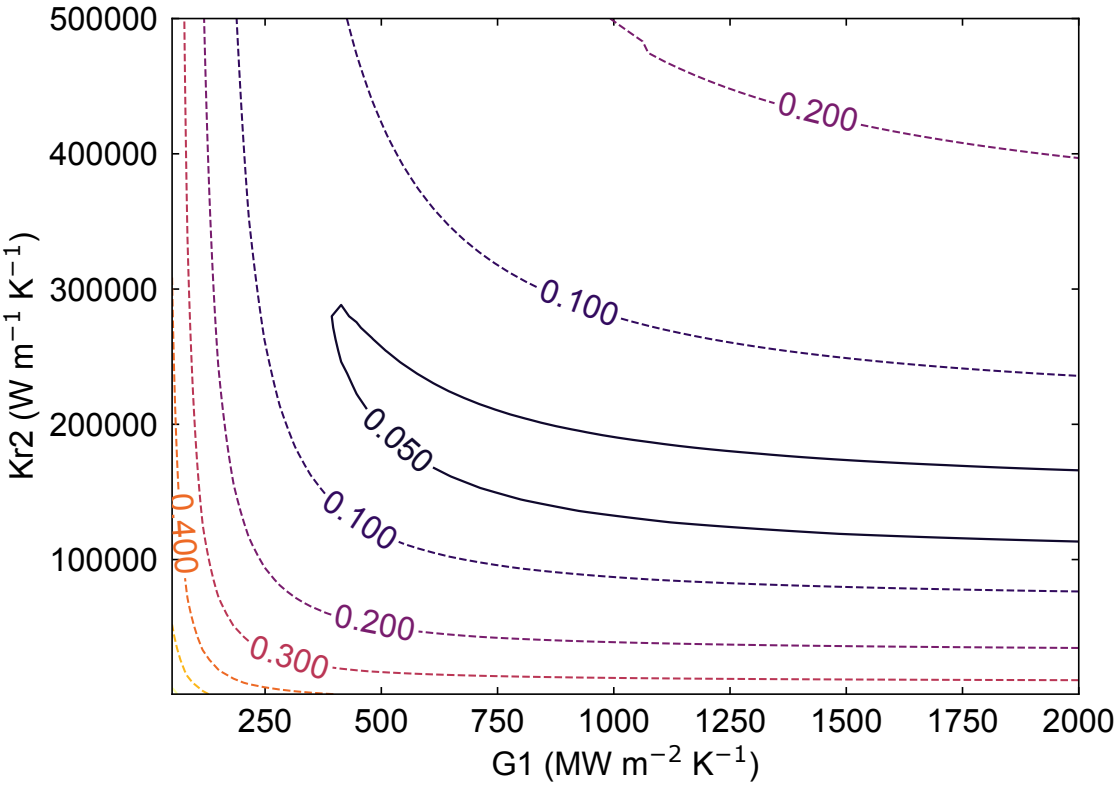

Figure S9: The Contour Uncertainty associated with the analytical model for approximating TBCs showing a lack of sensitivity to high TBCs >500.

Table S3: Values used for our POS model of Au-HBN. The optical phonon heat capacity for HBN was estimated assuming a Debye model for heat capacity and using a phonon dispersion found in literature[1]*. The thermal conductivity of HBN is defined as the geometric mean of the cross plane and in-plane thermal conductivities,* $\sqrt{\kappa_r \kappa_z}$*.*[8,21] *The polariton boundary conductance (PBC) was determined from fitting with an initial value of 1e9 W* $m^{-2}K^{-1}$*.*

	k_{cross} [W m^{-1} K^{-1}]	C [J m^3 K^{-1}]	h_{AU-HBN} [W m^{-2} K^{-1}]
Au	N/A	2.5e6[20]	1e9[FIT]
HBN	3.5[8]	1.28e6[1]	N/A

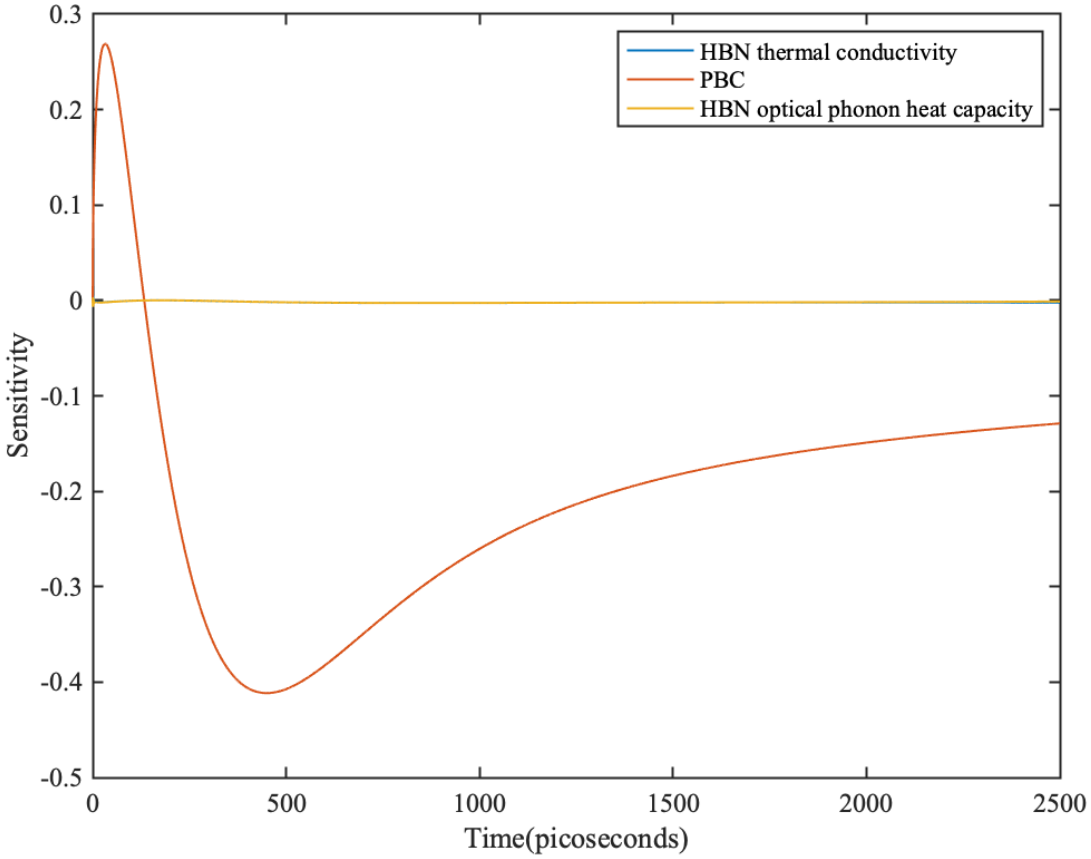

Figure S10: Here we show sensitivities of the boron nitride temperature response to the thermal conductivity of boron nitride, polaritonic boundary conductance, and the heat capacity of boron nitride respectively calculated by methods of Ref. [17]. *We have high sensitivity to polaritonic boundary conductance at all times, whereas both the thermal conductivity and heat capacity of boron nitride only have slight sensitivities at early times.*

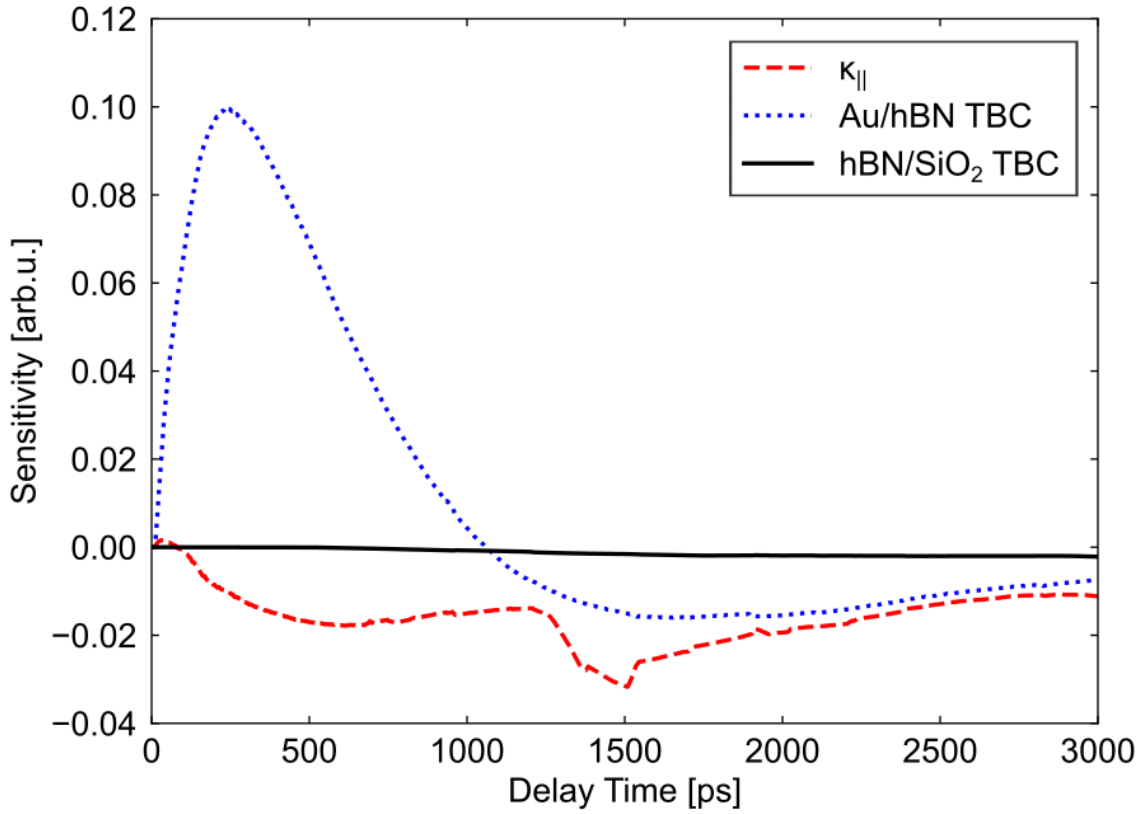

Figure S11: ***Sensitivity of TBC with respect to time delay using a Finite element model.*** *The thermoreflectance signal remains sensitive to the Au/hBN TBC well beyond the maximum signal even retaining the adiabatic condition on the surface of the hBN. The main effect of this parameter is shown by the maximum of the sensitivity curve, and by inspection an enhanced TBC results in a faster rate of heating with respect to the hBN. Even by comparison to the other thermal parameters of the stack the in plane thermal conductance and Au/hBN TBC are the most sensitive parameters.*

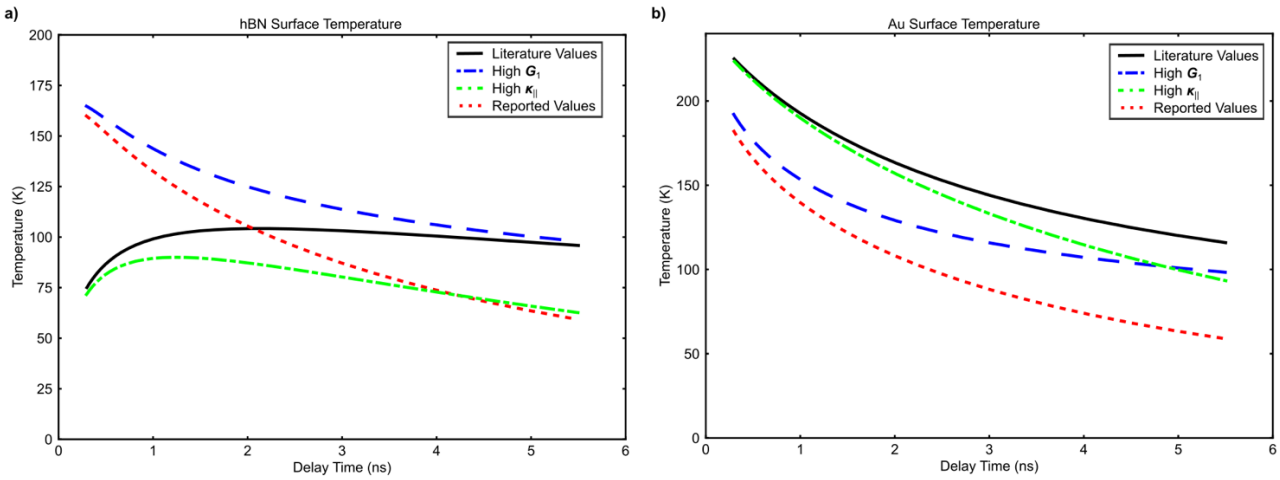

Figure S12: The calculated temperature vs time graphs predicted by the analytical model under experimental conditions. The maximum temperature rise in the hBN is predicted to be 80K under using the reported values from the main text. Without the high TBC (G_1), the curvature did not match the concavity in the measurements, and the high in-plane conductance ($\kappa_{||}$) serves to bring the general shape at long (>1ns) times.

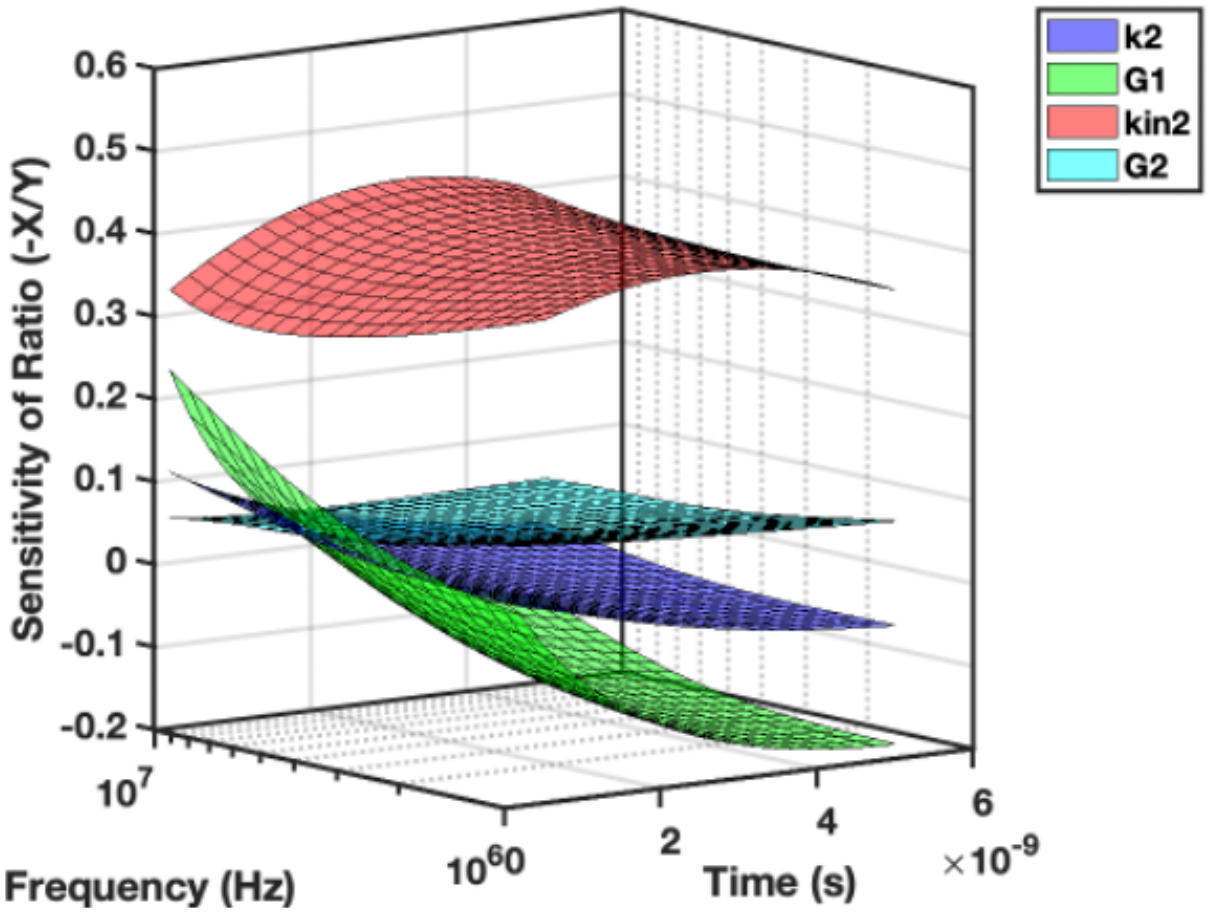

Figure S13: A plot showing the sensitivity to thermal parameters of the stack measured within the time and frequency range of interest5.

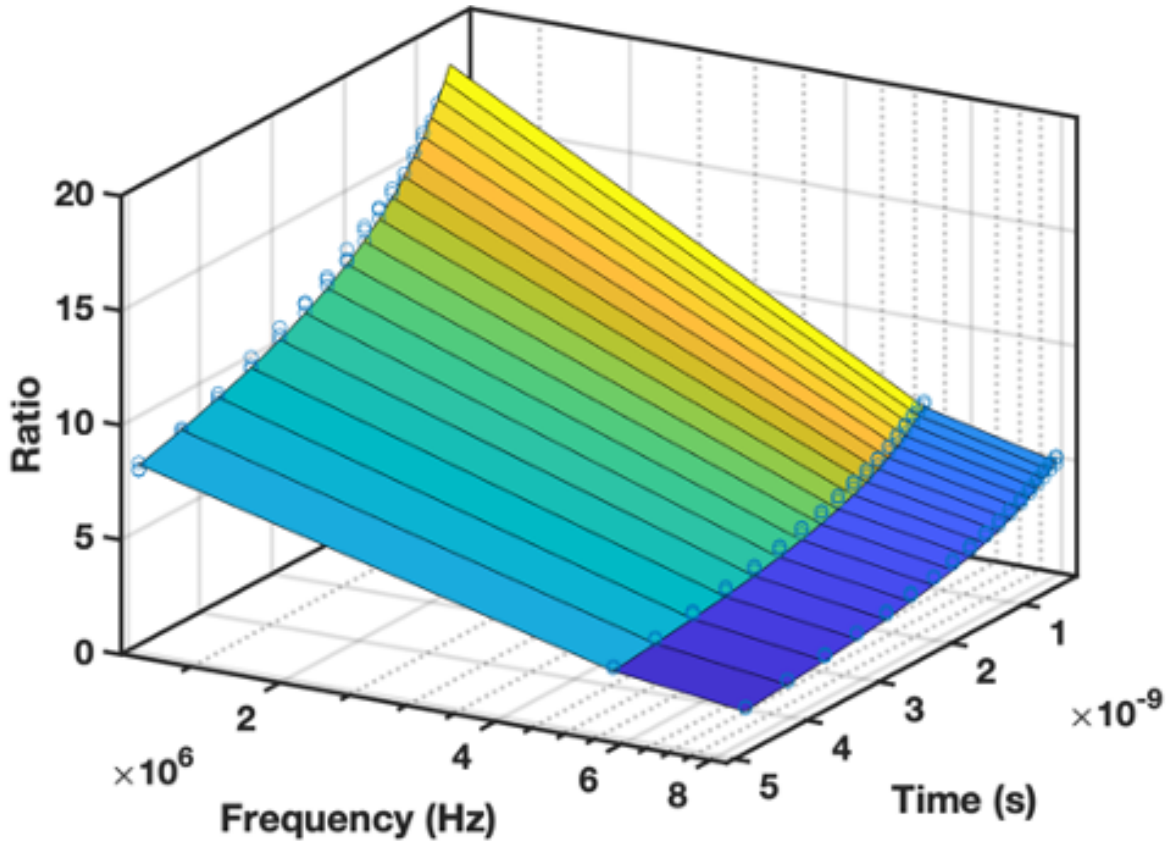

Figure S14: The fitted contour of the TDTR measurements averaged over three scans per modulation frequency.

Table S4: Values used for our TDTR fit of Au-HBN thermal stack. The gold thermal conductivity was measured with a four-point probe station averaging over 10 measurements. Both hBN and Au thicknesses were measured via AFM. The thermal boundary conductance (TBC) was determined from fitting with an initial value of 20e6 W $m^{-2}K^{-1}$.

	k_{in} [W m^{-1} K^{-1}]	C [J m^3 K^{-1}]	h_{AU-HBN} [W m^{-2} K^{-1}]	d[m]
Au	$209^{MEASURED}$	$2.5e6^{20}$	$12.3e6±2.3e6^{FIT}$	$47e\text{-}9^{MEASURED}$
HBN	$748±170.2^{FIT}$	$1.55e6^{22}$	N/A	$118e\text{-}9^{MEASURED}$

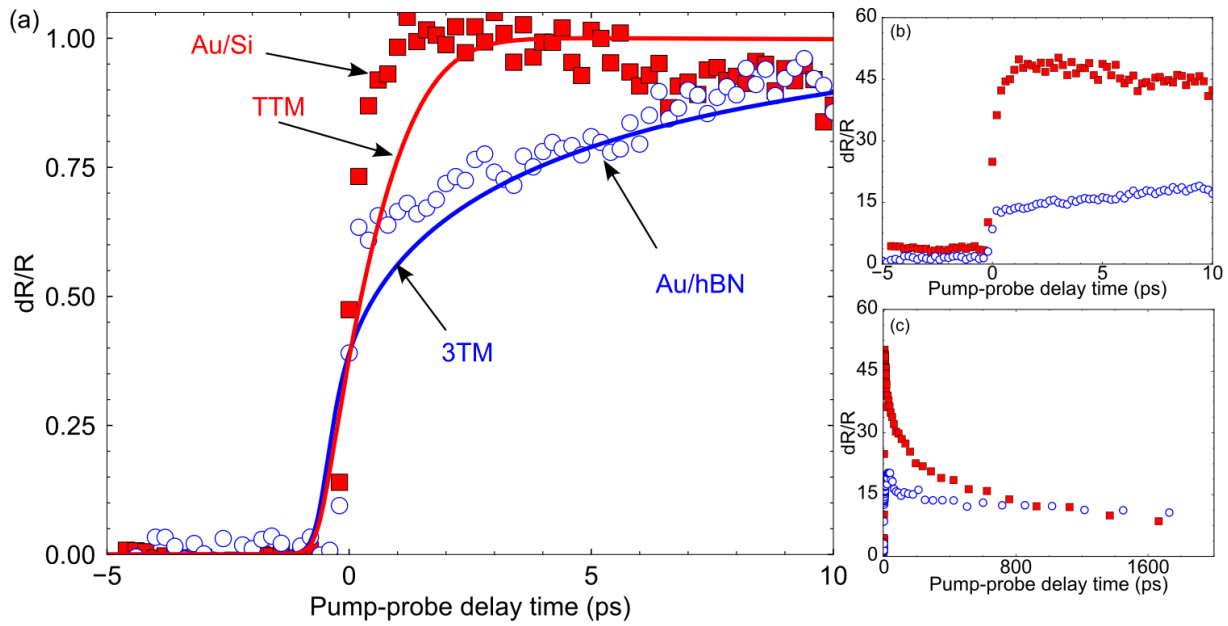

Figure S15. Ultrafast pump-probe response of Au on silicon and hBN substrates using a 520 nm pump and 2.1 um probe. At this probe wavelength, the Drude response of the thermoreflectivity of the probe results in sensitivity to the lattice temperature changes in the Au [23,24] (a) The transient lattice temperature changes in Au when on a Si substrate to those when on an hBN substrate, the Au lattice temperature changes on hBN during and after the 520-nm pump heating are suppressed at shorter pump-probe delay times and take longer to rise and equilibrate when coupling to the excited electrons in the Au. This is due to an additional energy loss pathway of the hot electrons in the Au to the hBN substrate, the trends of which we capture with a three-temperature model (3TM) that accounts for a gold electron to hBN HPhP/optical phonon energy transport pathway, shown in (a) assuming this pathway's thermal boundary conductance is 500 MW m^{-2} K^{-1}. Note, these ultrafast Au thermoreflectance trends are not captured with a two-temperature model (TTM), which shows a much faster lattice temperature rise when this Au electron-to-substrate thermal boundary conductance is not considered. (b) Un-

normalized thermoreflectance signal from the data presented in (a), where the reduced magnitude in the signal indicates the enhanced cooling of the Au electrons. (c) Thermal transience of the Au transducer, showing the return to standard diffusive processes beyond e-p non-equilibrium.

F. References

1. Giles, A. J. *et al.* Ultralow-loss polaritons in isotopically pure boron nitride. *Nat Mater* **17**, 134–139 (2018).
2. Vuong, T. Q. P. *et al.* Isotope engineering of van der Waals interactions in hexagonal boron nitride. *Nature Materials 2017 17:2* **17**, 152–158 (2017).
3. Liu, S. *et al.* Single Crystal Growth of Millimeter-Sized Monoisotopic Hexagonal Boron Nitride. *Chemistry of Materials* **30**, 6222–6225 (2018).
4. Wilson, R. B. *et al.* Thermoreflectance of metal transducers for optical pump-probe studies of thermal properties. *Optics Express, Vol. 20, Issue 27, pp. 28829-28838* **20**, 28829–28838 (2012).
5. Hao, J. & Zhou, L. Electromagnetic wave scatterings by anisotropic metamaterials: Generalized 4×4 transfer-matrix method. *Phys Rev B Condens Matter Mater Phys* **77**, (2008).
6. Olmon, R. L. *et al.* Optical dielectric function of gold. *Phys Rev B Condens Matter Mater Phys* **86**, (2012).
7. Cahill, D. G. Analysis of heat flow in layered structures for time-domain thermoreflectance. *Review of Scientific Instruments* **75**, 5119–5122 (2004).
8. Jiang, P., Qian, X., Yang, R. & Lindsay, L. Anisotropic thermal transport in bulk hexagonal boron nitride. *Phys Rev Mater* **2**, (2018).
9. Chen, J. K., Tzou, D. Y. & Beraun, J. E. A semiclassical two-temperature model for ultrafast laser heating. *Int J Heat Mass Transf* **49**, 307–316 (2006).
10. Qiu, T. Q. & Tient, C. L. Femtosecond laser heating of multi-layer metals-I. Analysis Femtosecond laser heating of multi-layer metals-I. Analysis. *Article in International Journal of Heat and Mass Transfer* **37**, 994 (1994).

11. Hohlfeld, J. *et al.* Electron and lattice dynamics following optical excitation of metals. *Chem Phys* **251**, 237–258 (2000).

12. Hopkins, P. E., Norris, P. M. & Stevens, R. J. Influence of inelastic scattering at metal-dielectric interfaces. *J Heat Transfer* **130**, (2008).

13. Wang, W. & Cahill, D. G. Limits to Thermal Transport in Nanoscale Metal Bilayers due to Weak Electron-Phonon Coupling in Au and Cu. (2012) doi:10.1103/PhysRevLett.109.175503.

14. Wang, L., Cheaito, R., Braun, J. L., Giri, A. & Hopkins, P. E. Thermal conductivity measurements of non-metals via combined time- and frequency-domain thermoreflectance without a metal film transducer. *Review of Scientific Instruments* **87**, 094902 (2016).

15. Smits, F. M. Measurement the of Sheet Resistivities Four-Point Probe. *The Bell System Technical Journal* **37**, 711–718 (1958).

16. Kittel, C. *Introduction to Solid State Physics*. (Jhon Wiley & Sons, 1996).

17. Schmidt, A. J., Cheaito, R. & Chiesa, M. A frequency-domain thermoreflectance method for the characterization of thermal properties. *Rev. Sci. Instrum* **80**, 94901 (2009).

18. Francoeur, M. & Pinar Mengüç, M. Role of fluctuational electrodynamics in near-field radiative heat transfer. *J Quant Spectrosc Radiat Transf* **109**, 280–293 (2008).

19. Francoeur, M., Pinar Mengüç, M. & Vaillon, R. Solution of near-field thermal radiation in one-dimensional layered media using dyadic Green's functions and the scattering matrix method. *J Quant Spectrosc Radiat Transf* **110**, 2002–2018 (2009).

20. Tomko, J. A., Kumar, S., Sundararaman, R. & Hopkins, P. E. Temperature dependent electron-phonon coupling of Au resolved via lattice dynamics measured with sub-picosecond infrared pulses. *J Appl Phys* **129**, (2021).

21. Braun, J. L., Olson, D. H., Gaskins, J. T. & Hopkins, P. E. A steady-state thermoreflectance method to measure thermal conductivity. *Review of Scientific Instruments* **90**, 024905 (2019).

22. Yuan, C. *et al.* Modulating the thermal conductivity in hexagonal boron nitride via controlled boron isotope concentration. *Communications Physics 2019 2:1* **2**, 1–8 (2019).

23. Tomko, J. A., Kumar, S., Sundararaman, R. & Hopkins, P. E. Temperature dependent electron-phonon coupling of Au resolved via lattice dynamics measured with sub-picosecond infrared pulses. *J. Appl. Phys.* **129**, (2021).

24. Hirt, D. *et al.* Increased thermal conductivity and decreased electron–phonon coupling factor of the aluminum scandium intermetallic phase (Al3Sc) compared to solid solutions. *Appl. Phys. Lett.* **124**, 202202 (2024).

25. Guo, L., Hodson, S. L., Fisher, T. S. & Xu, X. Heat Transfer Across Metal-Dielectric Interfaces During Ultrafast-Laser Heating. *J. Heat Transf.* **134**, (2012).

26. Hopkins, P. E., Kassebaum, J. L. & Norris, P. M. Effects of electron scattering at metal-nonmetal interfaces on electron-phonon equilibration in gold films. *J. Appl. Phys.* **105**, 023710 (2009).

27. Choi, G.-M., Moon, C.-H., Min, B.-C., Lee, K.-J. & Cahill, D. G. Thermal spin-transfer torque driven by the spin-dependent Seebeck effect in metallic spin-valves. *Nat. Phys.* **11**, 576–581 (2015).